

A STABLE HIGH-ORDER METHOD FOR TWO-DIMENSIONAL BOUNDED-OBSTACLE SCATTERING*

DAVID P. NICHOLLS[†] AND JIE SHEN[‡]

Abstract. A stable and high-order method for solving the Helmholtz equation on a two-dimensional domain exterior to a bounded obstacle is developed in this paper. The method is based on a boundary perturbation technique (“transformed field expansions”) coupled with a well-conditioned high-order spectral-Galerkin solver. The method is further enhanced with numerical analytic continuation, implemented via Padé approximation. Ample numerical results are presented to show the accuracy, stability, and versatility of the proposed method.

Key words. electromagnetic scattering, acoustic scattering, high-order methods, boundary perturbations, spectral-Galerkin methods

AMS subject classifications. 78A45, 65N35, 35J05, 41A58

DOI. 10.1137/050632920

1. Introduction. A wide variety of numerical techniques have been proposed for the approximation of electromagnetic and acoustic scattering returns from irregular obstacles (see, e.g., the book of Colton and Kress [9] and the survey papers of Warnick and Chew [35] and Reitich and Tamma [28]). Among the most compelling of these methods are those based on boundary perturbations, which can be originally traced to the work of Rayleigh [27] and Rice [29]. These methods are simple to implement, extremely fast, and quite robust within their domain of applicability. These properties have led to not only low- and high-order implementations of these boundary perturbation algorithms, but also questions regarding their convergence, conditioning, and accuracy.

In a series of recent papers, Bruno and Reitich [3], Nicholls and Nigam [20], and Nicholls and Reitich [24, 25] have rigorously shown that not only are the scattered (acoustic/electromagnetic) fields *analytic* functions of the grating height (slope) parameter, ε , but also they can be analytically continued for any real value of ε . These analytical results demonstrate the convergence of boundary perturbation expansions, and would appear to justify the classical algorithms of Rayleigh [27] and Rice [29] (pursued to higher orders by Bruno and Reitich [4, 5, 6, 7, 8]; see also Milder [14, 15, 17, 16] and others [18, 19, 12]). However, it was shown in [24, 25] that, in fact, these approaches rely on significant *cancellations* for their convergence. Consequently these numerical implementations are highly ill-conditioned when pursued to high order, as demonstrated in [24] and, to a more limited extent, section 3.4 of the current work.

A new boundary perturbation algorithm, advocated in [25] and specified in section 2.3, which overcomes this issue of poor conditioning, follows the perturbation philosophy of Rayleigh [27] and Rice [29] *preceded* by a change of variables, which

*Received by the editors June 1, 2005; accepted for publication (in revised form) February 10, 2006; published electronically August 16, 2006.

<http://www.siam.org/journals/sisc/28-4/63292.html>

[†]Department of Mathematics, University of Notre Dame, Notre Dame, IN 46556 (Nicholls.2@nd.edu). The work of this author was supported by the NSF through grants DMS-0139822 and DMS-0406007.

[‡]Department of Mathematics, Purdue University, West Lafayette, IN 47907 (shen@math.purdue.edu). The work of this author was supported by the NSF through grants DMS-0243191 and DMS-0311915.

“flattens” the shape of the scatterer to a flat configuration. This “transformed field expansions” (TFE) method proves to be not only accurate and stable, but also robust at high order, and provides reliable estimates of both near- and far-field information.

The purpose of the current research is to extend the work of Nicholls and Reitich [24, 25] in several important directions. First, we present the TFE algorithm in the setting of bounded-obstacle scattering problems, which, while related to grating scattering problems, present their own difficulties. Such difficulties include, e.g., the different nature of solutions reflected in the appearance of Hankel functions rather than complex exponential functions in the fundamental solution, and the algorithmic challenges presented by the singular nature of the Laplacian in polar coordinates.

Second, and perhaps most importantly, we construct a new, highly efficient and accurate, well-conditioned spectral-Galerkin solver for the Helmholtz equation in an annulus (with a boundary condition involving the Dirichlet–Neumann operator (DNO)), which needs to be solved repeatedly in the TFE algorithm. This solver is highly efficient and accurate since it takes advantage of the fact that the DNO, although global in physical space, is local in frequency space. Hence, we can reduce the two-dimensional problem into a sequence of one-dimensional problems with a spectrally accurate approximation to the DNO. This solver is also well-conditioned since, as is done in a series of papers [30, 31, 32, 33], we construct basis functions which lead to sparse and well-conditioned linear systems. The good conditioning properties of this new method allow us to investigate the behavior of the TFE algorithm as the frequency of scattered radiation is varied from low to moderate, which is the final extension we present. Furthermore, based upon the preliminary investigations of [34] for radially symmetric scatterers, we can speculate that this new method will be quite effective in simulating problems with high frequencies (though it is not “specially designed” for this setting; see, e.g., [2] for a high-frequency boundary integral method). However, such calculations quickly become quite large and time-consuming, and we focus, in this first phase of this project, on modest calculations that illustrate the fundamental properties of the TFE algorithm in the bounded-obstacle configuration.

In section 2.1 we review the equations which govern the scattering of electromagnetic and acoustic radiation from bounded obstacles in two dimensions. In section 2.2 we review the classical “field expansions” (FE) method for numerically computing scattering returns, and in section 2.3 we generalize the stabilized TFE algorithm to bounded-obstacle configurations. In section 2.4 we discuss new algorithmic enhancements that improve the conditioning properties of the TFE method, and in section 3 we present numerical results that display the properties of both the classical FE and stabilized TFE approaches. In particular, in section 3.4 we exhibit the instabilities present in the FE method due to cancellations which are no longer present in the new, TFE recursions. In section 4 we examine the behavior of the TFE algorithm for computing plane-wave scattering problems in a variety of scenarios. After recalling how Padé approximation can be brought to bear on such problems in section 4.1, we conclude in section 4.2 with a series of numerical experiments that illuminate the capabilities of this new TFE algorithm. We present concluding remarks and future directions in section 5.

2. Boundary perturbation methods. In this study we will focus on the problem of approximating electromagnetic and acoustic plane-wave scattering returns from bounded obstacles. For simplicity we restrict our attention to the scalar case in two dimensions, and leave the more general three-dimensional setting for future work. In this section we state the governing equations and notations of bounded-obstacle

scattering and recall a classical boundary perturbation algorithm. To conclude we derive a new, stabilized method, and then discuss numerical implementation issues.

2.1. Governing equations. We consider a two-dimensional time-harmonic acoustic or electromagnetic plane wave,

$$\tilde{v}_i(r, \theta, t) = e^{i\omega t} v_i(r, \theta) = e^{i\omega t} e^{ir(\alpha \cos(\theta) - \beta \sin(\theta))},$$

which is incident upon a bounded obstacle

$$\Sigma = \{(r, \theta) : 0 \leq r < a + g(\theta), 0 \leq \theta < 2\pi\}$$

and generates a scattered field

$$\tilde{v}_s(r, \theta, t) = e^{i\omega t} v_s(r, \theta).$$

Here $\tilde{v} = \tilde{v}_i + \tilde{v}_s$ denotes the pressure in acoustics or the component of the electric or magnetic field parallel to the invariant (z) direction in electromagnetics. The reduced scattered field, v_s , obeys the Helmholtz equation

$$(2.1) \quad \Delta v_s + k^2 v_s = 0, \quad (r, \theta) \in \Omega,$$

where

$$\Omega = \{(r, \theta) : r > a + g(\theta), 0 \leq \theta < 2\pi\},$$

and the wavenumber k satisfies

$$k^2 = \alpha^2 + \beta^2 = (2\pi/\lambda)^2,$$

where λ is the wavelength of the radiation. Of course the scattered field must be periodic in θ , but there are several physically relevant boundary conditions that can be specified at the surface of the object. For definiteness we work with a pressure release (acoustics) or perfectly conducting (TE in electromagnetics) surface where

$$(2.2) \quad v_s(a + g(\theta), \theta) = -v_i(a + g(\theta), \theta) = -e^{i(a+g(\theta))(\alpha \cos(\theta) - \beta \sin(\theta))}.$$

Finally, the scattered solution must satisfy the Sommerfeld radiation condition (SRC) to guarantee a physical solution,

$$(2.3) \quad \lim_{r \rightarrow \infty} r^{1/2} (\partial_r v_s - ik v_s) = 0.$$

Gathering equations (2.1), (2.2), and (2.3); denoting v_s by v ; and giving the Dirichlet data, (2.2), the generic name ξ , we state the fundamental equations of two-dimensional time-harmonic bounded-obstacle scattering:

$$(2.4a) \quad \Delta v + k^2 v = 0, \quad (r, \theta) \in \Omega,$$

$$(2.4b) \quad v(a + g(\theta), \theta) = \xi(\theta),$$

$$(2.4c) \quad \lim_{r \rightarrow \infty} r^{1/2} (\partial_r v - ikv) = 0.$$

An equivalent statement of this problem, which not only conveniently expresses the SRC but also poses the problem on a *bounded* domain, can be made in terms of the DNO, also called the Dirichlet-to-Neumann (DtN) map. Let $b > a + |g|_{L^\infty}$; then,

using a classical argument of separation of variables, the general solution of (2.4a) and (2.4c) for $r \geq b$ can be expressed as

$$v(r, \theta) = \sum_{p=-\infty}^{\infty} a_p H_p^{(1)}(kr) e^{ip\theta},$$

where $H_p^{(1)}$ is the p th Hankel function of the first kind. Therefore, if $v(b, \theta)$ is given,

$$v(b, \theta) = \psi(\theta) = \sum_{p=-\infty}^{\infty} \hat{\psi}_p e^{ip\theta},$$

the coefficients $\{a_p\}$ can be uniquely determined; namely, we have

$$v(r, \theta) = \sum_{p=-\infty}^{\infty} \hat{\psi}_p \frac{H_p^{(1)}(kr)}{H_p^{(1)}(kb)} e^{ip\theta}.$$

We define a DNO, T , by

$$(2.5) \quad T \psi \equiv \partial_r v(b, \theta) = \sum_{p=-\infty}^{\infty} k \frac{d_z H_p^{(1)}(kb)}{H_p^{(1)}(kb)} \hat{\psi}_p e^{ip\theta},$$

where

$$d_z H_p^{(1)}(kb) = \left. \frac{dH_p^{(1)}(z)}{dz} \right|_{z=kb},$$

which takes Dirichlet data, ψ , to Neumann data, $\partial_r v|_{r=b}$. Thus, (2.4) can be equivalently restated as

$$(2.6a) \quad \Delta v + k^2 v = 0, \quad (r, \theta) \in \Omega_{a+g,b},$$

$$(2.6b) \quad v(a + g(\theta), \theta) = \xi(\theta),$$

$$(2.6c) \quad \partial_r v(b, \theta) - T v(b, \theta) = 0,$$

where

$$\Omega_{a+g,b} = \{(r, \theta) : a + g(\theta) < r < b, 0 \leq \theta < 2\pi\}.$$

2.2. Field expansions. Considering a sufficiently smooth boundary deformation of the form $g(\theta) = \varepsilon f(\theta)$, it is known [3, 20, 24, 25] that the field, v , depends analytically on the parameter ε ; i.e., we have the strongly convergent expansion

$$v(r, \theta; \varepsilon) = \sum_{n=0}^{\infty} v_n(r, \theta) \varepsilon^n.$$

This observation serves as the basis for the method of “field expansions” (FE); see [7, 8] and the references therein. This algorithm consists of finding $\{v_n\}$ recursively by solving a sequence of Helmholtz problems in the unperturbed domain

$$\Omega_{a,b} = \{(r, \theta) : a < r < b, 0 \leq \theta < 2\pi\}.$$

More precisely, it is not hard to derive from (2.6) that the v_n must satisfy

$$(2.7a) \quad \Delta v_n + k^2 v_n = 0, \quad (r, \theta) \in \Omega_{a,b},$$

$$(2.7b) \quad v_n(a, \theta) = R_n(\theta),$$

$$(2.7c) \quad \partial_r v_n(b, \theta) - T v_n(b, \theta) = 0,$$

where

$$(2.7d) \quad R_n(\theta) = \delta_{n,0} \xi(\theta) - \sum_{l=0}^{n-1} \frac{f^{n-l}}{(n-l)!} \partial_r^{n-l} v_l(a, \theta)$$

and $\delta_{n,m}$ is the Kronecker delta. Equations (2.7a) and (2.7c) imply that

$$(2.8) \quad v_n(r, \theta) = \sum_{p=-\infty}^{\infty} d_{n,p} \frac{H_p^{(1)}(kr)}{H_p^{(1)}(ka)} e^{ip\theta},$$

while (2.7b) provides a recursion for the $d_{n,p}$. At order zero, $d_{0,p} = \hat{\xi}_p$, the p th Fourier coefficient of $\xi(\theta)$, and for $n > 0$

$$(2.9) \quad d_{n,p} = - \sum_{l=0}^{n-1} \sum_{q=-\infty}^{\infty} C_{n-l,p-q} \frac{d_z^{n-l} H_q^{(1)}(ka)}{H_q^{(1)}(ka)} d_{l,q},$$

where the $C_{l,q}$ are defined by

$$\frac{(kf)^l}{l!} = \sum_{q=-\infty}^{\infty} C_{l,q} e^{iq\theta}.$$

Provided that we truncate the number of Fourier coefficients in f and retain only a finite number of terms $d_{l,p}$ (say, $0 \leq l \leq N$ and $-N_\theta/2 \leq p \leq N_\theta/2 - 1$), we have completely specified the *numerical* FE algorithm with (2.9). The only detail remaining is that the convolution product appearing in (2.9) is performed via FFT acceleration.

2.3. Transformed field expansions. As we shall see in section 3.4, the FE method outlined above suffers from severe ill-conditioning due to significant cancellations which occur in the recursion (2.9). However, a simple change of variables coupled to the FE design philosophy leads to a *stable*, high-order boundary perturbation scheme we call “transformed field expansions” (TFE) [21, 22, 23, 20, 24, 25]. The change of variables

$$r' = \frac{(b-a)r - bg(\theta)}{(b-a) - g(\theta)} = \frac{dr - bg}{d - g}, \quad \theta' = \theta,$$

where $d = (b-a)$, maps the perturbed geometry $\Omega_{a+g,b}$ to the annulus $\Omega_{a,b}$. We now seek to restate (2.6) in these transformed coordinates. We note that

$$(2.10a) \quad (d - g(\theta)) \partial_\theta = (d - g(\theta')) \partial_{\theta'} - B(r', \theta') \partial_{r'},$$

$$(2.10b) \quad (d - g(\theta)) \partial_r = d \partial_{r'},$$

$$(2.10c) \quad (d - g(\theta)) D_r = d D_{r'} + A(r', \theta') \partial_{r'},$$

where $D_r = r\partial_r$,

$$A(r', \theta') = g(\theta')(b - r'),$$

and

$$B(r', \theta') = \partial_{\theta'} A = (\partial_{\theta'} g(\theta'))(b - r');$$

we note for future reference that

$$d r = d r' + A(r', \theta').$$

To begin the transformation we start with the Helmholtz equation, (2.6a):

$$\begin{aligned} 0 &= \Delta v + k^2 v = r^2 \Delta v + r^2 k^2 v \\ &= D_r^2 v + \partial_{\theta'}^2 v + r^2 k^2 v \\ &= (d-g)^2 D_r^2 v + (d-g)^2 \partial_{\theta'}^2 v + (d-g)^2 r^2 k^2 v \\ &= [(d-g)D_r][(d-g)D_r]v + [(d-g)\partial_{\theta'}][(d-g)\partial_{\theta'}]v \\ (2.11) \quad &+ (\partial_{\theta'} g)[(d-g)\partial_{\theta'}]v + (d-g)^2 r^2 k^2 v. \end{aligned}$$

Writing

$$u(r', \theta') = v(r' + A/d, \theta')$$

and replacing v in (2.11) by u , we obtain

$$\begin{aligned} 0 &= [dD_{r'} + A\partial_{r'}][dD_{r'} + A\partial_{r'}]u + [(d-g)\partial_{\theta'} - B\partial_{r'}][(d-g)\partial_{\theta'} - B\partial_{r'}]u \\ &\quad + (\partial_{\theta'} g)[(d-g)\partial_{\theta'} - B\partial_{r'}]u + (d-g)^2 (r' + A/d)^2 k^2 u \\ &= d^2 D_{r'}^2 u + dA\partial_{r'} D_{r'} u + dD_{r'} [A\partial_{r'} u] + A\partial_{r'} [A\partial_{r'} u] \\ &\quad + d^2 \partial_{\theta'}^2 u - dg\partial_{\theta'}^2 u - d\partial_{\theta'} [g\partial_{\theta'} u] + g\partial_{\theta'} [g\partial_{\theta'} u] - dB\partial_{r'} \partial_{\theta'} u + B\partial_{r'} [g\partial_{\theta'} u] \\ &\quad - d\partial_{\theta'} [B\partial_{r'} u] + g\partial_{\theta'} [B\partial_{r'} u] + B\partial_{r'} [B\partial_{r'} u] \\ &\quad + d(\partial_{\theta'} g)\partial_{\theta'} u - g(\partial_{\theta'} g)\partial_{\theta'} u - (\partial_{\theta'} g)B\partial_{r'} u \\ &\quad + d^2 (r')^2 k^2 u + \sum_{j=1}^4 C_j(g) k^2 u, \end{aligned}$$

where

$$\begin{aligned} C_1(g) &= -2d g(r')^2 + 2d A r', \\ C_2(g) &= g^2(r')^2 - 4g A r' + A^2, \\ C_3(g) &= (2/d) A g^2 r' - (2/d) g A^2, \\ C_4(g) &= (1/d^2) g^2 A^2. \end{aligned}$$

We rewrite this as

$$D_{r'}^2 u + \partial_{\theta'}^2 u + (r')^2 k^2 u = F(r', \theta'; u),$$

where

$$\begin{aligned} -d^2 F &= dA\partial_{r'} D_{r'} u + dD_{r'} [A\partial_{r'} u] + A\partial_{r'} [A\partial_{r'} u] \\ &\quad - dg\partial_{\theta'}^2 u - d\partial_{\theta'} [g\partial_{\theta'} u] + g\partial_{\theta'} [g\partial_{\theta'} u] - dB\partial_{r'} \partial_{\theta'} u + B\partial_{r'} [g\partial_{\theta'} u] \\ &\quad - d\partial_{\theta'} [B\partial_{r'} u] + g\partial_{\theta'} [B\partial_{r'} u] + B\partial_{r'} [B\partial_{r'} u] \\ &\quad + d(\partial_{\theta'} g)\partial_{\theta'} u - g(\partial_{\theta'} g)\partial_{\theta'} u - (\partial_{\theta'} g)B\partial_{r'} u + \sum_{j=1}^4 C_j(g) k^2 u. \end{aligned}$$

The Dirichlet condition, (2.6b), simply transforms to

$$u(a, \theta') = \xi(\theta'),$$

while (2.6c) can be written as

$$\begin{aligned} 0 &= \partial_r v(b, \theta) - T v(b, \theta) \\ &= (d - g) \partial_r v(b, \theta) - (d - g) T v(b, \theta) \\ &= d \partial_{r'} u(b, \theta') - d T' u(b, \theta') + g(\theta') T' u(b, \theta'). \end{aligned}$$

Since $T' = T$, (2.6c) transforms to

$$\partial_{r'} u(b, \theta') - T u(b, \theta') = J(\theta'),$$

where

$$d J(\theta') = -g(\theta') T u(b, \theta').$$

Collecting these transformations, we find that the transformed field u , upon dropping primes, satisfies

$$(2.12a) \quad D_r^2 u + \partial_\theta^2 u + r^2 k^2 u = F(r, \theta; u), \quad (r, \theta) \in \Omega_{a,b},$$

$$(2.12b) \quad u(a, \theta) = \xi(\theta),$$

$$(2.12c) \quad \partial_r u(b, \theta) - T u(b, \theta) = J(\theta).$$

Again, letting $g = \varepsilon f$, if f is sufficiently smooth, the analyticity of the *transformed* field u (see [20]) implies that

$$(2.13) \quad u(r, \theta; \varepsilon) = \sum_{n=0}^{\infty} u_n(r, \theta) \varepsilon^n.$$

Inserting the above into (2.12), it is straightforward, albeit tedious, to derive the following recursions for $\{u_n\}$:

$$(2.14a) \quad D_r^2 u_n + \partial_\theta^2 u_n + r^2 k^2 u_n = F_n(r, \theta), \quad (r, \theta) \in \Omega_{a,b},$$

$$(2.14b) \quad u_n(a, \theta) = \delta_{n,0} \xi(\theta),$$

$$(2.14c) \quad \partial_r u_n(b, \theta) - T u_n(b, \theta) = J_n(\theta),$$

where

$$\begin{aligned} -d^2 F_n &= d A \partial_{r'} D_{r'} u_{n-1} + d D_{r'} [A \partial_{r'} u_{n-1}] + A \partial_{r'} [A \partial_{r'} u_{n-2}] \\ &\quad - d f \partial_{\theta'}^2 u_{n-1} - d \partial_{\theta'} [f \partial_{\theta'} u_{n-1}] + f \partial_{\theta'} [f \partial_{\theta'} u_{n-2}] \\ &\quad - d B \partial_{r'} \partial_{\theta'} u_{n-1} + B \partial_{r'} [f \partial_{\theta'} u_{n-2}] \\ &\quad - d \partial_{\theta'} [B \partial_{r'} u_{n-1}] + f \partial_{\theta'} [B \partial_{r'} u_{n-2}] + B \partial_{r'} [B \partial_{r'} u_{n-2}] \\ &\quad + d (\partial_{\theta'} f) \partial_{\theta'} u_{n-1} - f (\partial_{\theta'} f) \partial_{\theta'} u_{n-2} - (\partial_{\theta'} f) B \partial_{r'} u_{n-2} \\ &\quad + \sum_{j=1}^4 C_j(f) k^2 u_{n-j} \end{aligned} \tag{2.14d}$$

and

$$(2.14e) \quad d J_n = -f T u_{n-1}(b, \theta).$$

In the derivation of (2.14d) it is important to remember that A and B depend *linearly* on g and therefore εf .

Remark 2.1. We note at this point the fundamentally inhomogeneous nature of (2.14). If we now wish to include effects from distributed sources, resulting in an inhomogeneous term—say, $M(r, \theta)$ —appearing on the right-hand side of (2.1), the only modification to our TFE algorithm is that M will appear as F_0 . By contrast, the FE recursions must be completely rederived, and even a boundary integral/element method will require a new implementation (though at the same computational cost).

2.4. TFE: Numerical implementation. It is clear from the above that the efficiency and accuracy of the TFE method depends greatly on how rapidly and accurately we can solve the Helmholtz equation (2.14a)–(2.14c) on an annular domain with the nonstandard outer boundary condition (expressed using a DNO). We now describe an efficient and accurate spectral-Galerkin method for the following problem (which is slightly more general than (2.14a)–(2.14c)):

$$(2.15a) \quad D_r^2 U + \partial_\theta^2 U + r^2 k^2 U = F, \quad (r, \theta) \in \Omega_0,$$

$$(2.15b) \quad U(a, \theta) = \xi(\theta),$$

$$(2.15c) \quad \partial_r U(b, \theta) - T U(b, \theta) = \eta(\theta),$$

where $F(r, \theta)$, $\xi(\theta)$, and $\eta(\theta)$ are given functions. Expanding $U(r, \theta)$, $F(r, \theta)$, $\xi(\theta)$, and $\eta(\theta)$ in Fourier series, e.g.,

$$(U(r, \theta), F(r, \theta)) = \sum_{p=-\infty}^{\infty} (\hat{u}_p(r), \hat{f}_p(r)) e^{ip\theta}, \quad (\xi(\theta), \eta(\theta)) = \sum_{p=-\infty}^{\infty} (\hat{\xi}_p, \hat{\eta}_p) e^{ip\theta},$$

and recalling the definition of the DNO in (2.5), we can decompose (2.15) into the following sequence of one-dimensional problems ($p = 0, \pm 1, \pm 2, \dots$):

$$(2.16a) \quad D_r^2 \hat{u}_p + (r^2 k^2 - p^2) \hat{u}_p = \hat{f}_p, \quad r \in (a, b),$$

$$(2.16b) \quad \hat{u}_p(a) = \hat{\xi}_p,$$

$$(2.16c) \quad \partial_r \hat{u}_p(b) - k \frac{d_z H_p^{(1)}(kb)}{H_p^{(1)}(kb)} \hat{u}_p(b) = \hat{\eta}_p.$$

It is known (see Lemma 3.2 in [10], and [11]) that

$$(2.17) \quad \begin{aligned} \operatorname{Im} \left\{ \frac{d_z H_p^{(1)}(kb)}{H_p^{(1)}(kb)} \right\} &> 0, & \operatorname{Re} \left\{ \frac{d_z H_p^{(1)}(kb)}{H_p^{(1)}(kb)} \right\} &< 0, \\ -\frac{d_z H_p^{(1)}(kb)}{H_p^{(1)}(kb)} &\sim \frac{p+1}{b} \quad \text{as } p \rightarrow \pm\infty, \end{aligned}$$

which enables the well-posedness of the problem (2.16) to be directly established.

We now describe a spectral-Galerkin method for (2.16). To this end, let us first make a change of variable $x = \frac{2(r-a)}{b-a} - 1$, which maps $r \in (a, b)$ to $x \in I \equiv (-1, 1)$. If we define

$$\begin{aligned} \tilde{u}_p(x) &= \hat{u}_p(r), & \tilde{f}_p(x) &= \hat{f}_p(r), & \tilde{\eta}_p &= \frac{b-a}{2} \hat{\eta}_p, & \tilde{\xi}_p &= \hat{\xi}_p, \\ c &= \frac{b+a}{b-a}, & \omega &= \frac{k(b-a)}{2}, & T_p &= k \frac{d_z H_p^{(1)}(kb)}{H_p^{(1)}(kb)}, \end{aligned}$$

then (2.16) becomes

$$(2.18a) \quad (x+c)\partial_x((x+c)\partial_x\tilde{u}_p) + ((x+c)^2\omega^2 - p^2)\tilde{u}_p = \tilde{f}_p, \quad x \in I,$$

$$(2.18b) \quad \tilde{u}_p(-1) = \tilde{\xi}_p,$$

$$(2.18c) \quad \partial_x\tilde{u}_p(1) - T_p\tilde{u}_p(1) = \tilde{\eta}_p.$$

One verifies easily that

$$h_p(x) = \frac{\tilde{\eta}_p + T_p\tilde{\xi}_p}{1 - 2T_p}x + \frac{\tilde{\eta}_p + \tilde{\xi}_p - T_p\tilde{\xi}_p}{1 - 2T_p}$$

satisfies the two boundary conditions in (2.18). Hence, setting

$$d = \frac{\tilde{\eta}_p + T_p\tilde{\xi}_p}{1 - 2T_p}, \quad f_p = \tilde{f}_p - ((x+c)^2\omega^2 - p^2)h_p - d(x+c),$$

$$\tilde{u}_p(x) = u_p(x) + h_p(x),$$

we can rewrite (2.18) into the following problem with homogeneous boundary conditions:

$$(2.19a) \quad (x+c)\partial_x((x+c)\partial_x u_p) + ((x+c)^2\omega^2 - p^2)u_p = f_p, \quad x \in I,$$

$$(2.19b) \quad u_p(-1) = 0,$$

$$(2.19c) \quad \partial_x u_p(1) - T_p u_p(1) = 0.$$

Let us denote by P_N the space of complex polynomials of degree less than or equal to N . We set

$$(2.20) \quad X_N^{(p)} = \{u \in P_N : u(-1) = 0, \partial_x u(1) - T_p u(1) = 0\}.$$

The spectral-Galerkin method for (2.19) is to find $u_N^{(p)} \in X_N^{(p)}$ such that

$$(2.21) \quad \int_I (x+c)\partial_x((x+c)\partial_x u_N^{(p)})\bar{v}_N \, dx + \int_I ((x+c)^2\omega^2 - p^2)u_N^{(p)}\bar{v}_N \, dx$$

$$= \int_I f_p\bar{v}_N \, dx \quad \forall v_N \in X_N^{(p)},$$

where \bar{v}_N is the complex conjugate of v_N .

The well-posedness of (2.21) follows from (2.16). However, a complete error analysis is still elusive. In [34], an error analysis was carried out for the case where T_p is replaced by its zeroth-order approximation, ip . The analysis was based on a new, uniform a priori estimate for the approximate solution. However, the extension of that procedure to the current situation appears to be subtle and is the subject of ongoing research.

We now describe an efficient numerical algorithm for solving (2.21). We recall that if T_p is a real number and P_N consists of real polynomials, it is shown in [30, 31] that there exist unique real pairs $(\alpha_k^{(p)}, \beta_k^{(p)})$ such that

$$X_N^{(p)} = \text{span}\{\phi_0^{(p)}, \phi_1^{(p)}, \dots, \phi_{N-2}^{(p)}\}$$

with $\phi_k^{(p)}(x) = L_k(x) + \alpha_k^{(p)}L_{k+1}(x) + \beta_k^{(p)}L_{k+2}(x)$; we recall that L_k is the k th Legendre polynomial. It is easy to see that this is still true if we allow $(\alpha_k^{(p)}, \beta_k^{(p)})$ to be complex

for complex T_p and $P_N, X_N^{(p)}$ as defined above. In fact, one verifies easily that

$$\alpha_k^{(p)} = \frac{(2k+3)}{(k+2)^2 - 2T_p}, \quad \beta_k^{(p)} = \alpha_k^{(p)} - 1.$$

We recall from (2.17) that $\text{Re}(T_p) < 0$; hence, $(\alpha_k^{(p)}, \beta_k^{(p)})$ are always well defined. Therefore, setting

$$\begin{aligned} u_N^{(p)} &= \sum_{j=0}^{N-2} u_j^{(p)} \phi_j, & \mathbf{u} &= (u_0^{(p)}, u_1^{(p)}, \dots, u_{N-2}^{(p)})^T, \\ a_{jl}^{(p)} &= \int_I (x+c) \partial_x ((x+c) \partial_x \phi_l^{(p)}) \bar{\phi}_j^{(p)} dx, & A^{(p)} &= (a_{jl}^{(p)}), \\ b_{jl}^{(p)} &= \int_I ((x+c)^2 \omega^2 - p^2) \phi_l^{(p)} \bar{\phi}_j^{(p)} dx, & B^{(p)} &= (b_{jl}^{(p)}), \\ f_j^{(p)} &= \int_I f_p \bar{\phi}_j^{(p)} dx, & \mathbf{f}^{(p)} &= (f_0^{(p)}, f_1^{(p)}, \dots, f_{N-2}^{(p)})^T, \end{aligned}$$

the system (2.21) becomes the following complex matrix equation:

$$(2.22) \quad (A^{(p)} + B^{(p)})\mathbf{u}^{(p)} = \mathbf{f}^{(p)}.$$

Thanks to the special form of $\phi_j^{(p)}$, we have that

$$b_{jl}^{(p)} = 0, \quad |j-l| > 4; \quad a_{jl}^{(p)} = 0, \quad l < j-2.$$

Hence, for each p , the linear system (2.22) can be solved in $\mathcal{O}(N^2)$ operations by using a direct Gaussian elimination process. Renaming N as N_r , the Fourier–Legendre approximation for (2.15) is given (with $x = \frac{2(r-a)}{b-a} - 1$) by

$$(2.23) \quad U_{N_r, N_\theta}(r, \theta) = \sum_{p=-N_\theta/2-1}^{N_\theta/2} \sum_{j=0}^{N_r-2} (u_j^{(p)} \phi_j^{(p)}(x) + h_p(x)) e^{ip\theta},$$

which is the solution of the following approximate variational problem:

$$(2.24a) \quad \begin{aligned} &-(r \partial_r U_{N_r, N_\theta}, \partial_r(rv)) - (\partial_\theta U_{N_r, N_\theta}, \partial_\theta v) \\ &+ k^2 (r^2 U_{N_r, N_\theta}, v) = (F, v) \quad \forall v \in V_{N_r, N_\theta}, \end{aligned}$$

$$(2.24b) \quad U_{N_r, N_\theta}(a, \theta) = \xi_{N_\theta}(\theta),$$

$$(2.24c) \quad (\partial_r - T_{N_\theta}) U_{N_r, N_\theta}(b, \theta) = \eta_{N_\theta}(\theta),$$

where

$$(2.25a) \quad V_{N_r, N_\theta} = \text{span}\{\phi_j^{(p)}(x(r)) e^{ip\theta} : -N_\theta/2 \leq p \leq N_\theta/2 - 1; 0 \leq j \leq N_r - 2\},$$

$$(2.25b) \quad (\xi_{N_\theta}(\theta), \eta_{N_\theta}(\theta)) = \sum_{p=-N_\theta/2}^{N_\theta/2-1} (\hat{\xi}_p, \hat{\eta}_p) e^{ip\theta},$$

$$(2.25c) \quad T_{N_\theta} \psi(\theta) = \sum_{p=-N_\theta/2}^{N_\theta/2-1} k \frac{d_z H_p^{(1)}(kb)}{H_p^{(1)}(kb)} \hat{\psi}_p e^{ip\theta} \quad \text{for } \psi(\theta) = \sum_{p=-\infty}^{\infty} \hat{\psi}_p e^{ip\theta}.$$

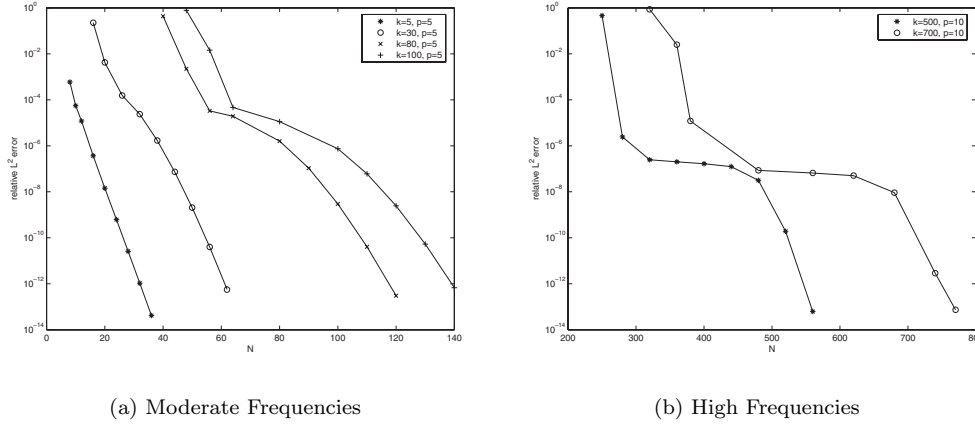


FIG. 2.1. Relative L^2 error versus N_r with $N_\theta = 20$, as compared to an exact solution.

The total cost for obtaining U_{N_r, N_θ} is $\mathcal{O}(N_r^2 N_\theta \log(N_\theta))$.

We now present some numerical results demonstrating the accuracy of the above scheme. As a test example, we consider the canonical problem (2.15) with $a = 1$, $b = 2$ and take

$$F(r, \theta) = 0, \quad \xi(\theta) = H_p^{(1)}(ka)e^{ip\theta}, \quad \eta(\theta) = 0.$$

In this case the exact solution is $U(r, \theta) = H_p^{(1)}(kr)e^{ip\theta}$. It is clear that for given p , $e^{ip\theta}$ can be exactly determined with $N_\theta \geq 2p$. Thus we will concentrate on the approximation behavior of our scheme with respect to the frequency k . In Figure 2.1, we present the relative L^2 error versus N_r for a wide range of frequencies. We note that for k relatively small, the errors quickly enter the asymptotic range and converge at an exponential rate. For moderate to large k , the errors exhibit an initial sharp drop at $N_r \sim k/2$, then decay slowly until $N_r \sim k$, and finally enter the asymptotic range, converging at an exponential rate. These results indicate that (i) the approximate solution U_{N_r, N_θ} will converge to the exact solution $U(r, \theta)$ exponentially fast as $N_r, N_\theta \rightarrow +\infty$, provided that all $F(r, \theta)$, $\xi(\theta)$, and $\eta(\theta)$ are analytic in Ω ; and (ii) our numerical scheme is stable for large N_r and capable of providing accurate results for large frequencies.

3. Numerical results: Comparison with an exact solution. In this section we present the results of a numerical experiment conducted with the two algorithms outlined above: the FE method of section 2.2 and the TFE method of section 2.3. We begin by outlining the diagnostic test (based upon an exact solution), which we have found useful in measuring the performance of these methods. We then describe how the FE algorithm suffers from severe numerical ill-conditioning, while the TFE approach is largely immune from such issues.

3.1. A diagnostic test. For the testing of numerical algorithms it is extremely useful to compare approximations with exact solutions whenever possible. In the case of scattering from a bounded obstacle, we consider again solutions of the form

$$(3.1) \quad v_p(r, \theta) = a_p H_p^{(1)}(kr)e^{ip\theta},$$

which satisfy (2.6a) and (2.6c). Given a profile $g(\theta) = \varepsilon f(\theta)$, we have a solution to (2.6), provided that we set

$$\xi(\theta) = \xi_p(\theta) = v_p(a + \varepsilon f(\theta), \theta).$$

So, provided with (ε, f, ξ_p) , both the FE and TFE algorithms deliver approximations to the field which can be compared with the exact field, v_p . Of course one need not compare the entire field and may choose, instead, to simply compare the field in the “near field” (at $r = a + \varepsilon f$) or the “far field” (at $r = b$). Additionally, derivatives of the field have physical interpretations and may be measured as well. In particular, the normal derivative of the field on a surface has the interpretation in electromagnetics as the current, and it is useful to measure this in both the near and far fields.

In this paper we focus on the most challenging computation mentioned above, the current at the surface of the obstacle; here the effects of the geometric perturbation are felt most strongly. We define this surface current as

$$\nu(\theta) = \nabla v|_{r=a+g} \cdot N_g,$$

where $N_g = ((a + g), -\partial_\theta g)^T$ is chosen unnormalized to match the definition of the DNO studied in Nicholls and Nigam [20] and Nicholls and Reitich [24, 25]. With this choice of normal it is easy to see that

$$(3.2) \quad \nu(\theta) = (a + g) \partial_r v|_{r=a+g} - \frac{(\partial_\theta g)}{(a + g)} \partial_\theta v|_{r=a+g}$$

so that, given (ε, f, ξ_p) , an *exact* current ν_p can be specified using (3.2) and compared with FE and TFE approximations.

3.2. Computation of the surface current: Field expansions. The FE approximation to the surface current can be generated by noting that (3.2), upon multiplication by $(a + g)$, can be rewritten as

$$\begin{aligned} \nu &= a \partial_r v|_{r=a+g} + 2g \partial_r v|_{r=a+g} + \frac{1}{a} g^2 \partial_r v|_{r=a+g} \\ &\quad - \frac{1}{a} (\partial_\theta g) \partial_\theta v|_{r=a+g} - \frac{1}{a} g \nu. \end{aligned}$$

Setting $g = \varepsilon f$, recalling our FE expansion, (2.8),

$$v(r, \theta, \varepsilon) = \sum_{n=0}^{\infty} \varepsilon^n \sum_{p=-\infty}^{\infty} d_{n,p} \frac{H_p^{(1)}(kr)}{H_p^{(1)}(ka)} e^{ip\theta},$$

and using the fact that $\nu(\theta, \varepsilon)$ is analytic in ε (see [20, 24, 25]),

$$\nu(\theta, \varepsilon) = \sum_{n=0}^{\infty} \nu_n(\theta) \varepsilon^n,$$

it is not difficult to see that

$$\begin{aligned}
 \nu_n &= (ak) \sum_{l=0}^n \frac{(kf)^l}{l!} \sum_{p=-\infty}^{\infty} \frac{d_z^{l+1} H_p^{(1)}(ka)}{H_p^{(1)}(ka)} d_{n-l,p} e^{ip\theta} \\
 &+ 2f \sum_{l=0}^{n-1} \frac{(kf)^l}{l!} \sum_{p=-\infty}^{\infty} \frac{d_z^{l+1} H_p^{(1)}(ka)}{H_p^{(1)}(ka)} d_{n-1-l,p} e^{ip\theta} \\
 &+ \frac{1}{a} f^2 \sum_{l=0}^{n-2} \frac{(kf)^l}{l!} \sum_{p=-\infty}^{\infty} \frac{d_z^{l+1} H_p^{(1)}(ka)}{H_p^{(1)}(ka)} d_{n-2-l,p} e^{ip\theta} \\
 &- \frac{1}{a} (\partial_\theta f) \sum_{l=0}^{n-1} \frac{(kf)^l}{l!} \sum_{p=-\infty}^{\infty} \frac{d_z^l H_p^{(1)}(ka)}{H_p^{(1)}(ka)} (ip) d_{n-1-l,p} e^{ip\theta} \\
 (3.3) \quad &- \frac{1}{a} f \nu_{n-1}.
 \end{aligned}$$

3.3. Computation of the surface current: Transformed field expansions. To use the TFE algorithm in a simulation of the current ν , (3.2), we perform the following manipulations:

$$\begin{aligned}
 (a+g)(d-g)\nu &= (a+g)^2(d-g) \partial_r v|_{r=a+g} - (\partial_\theta g)(d-g) \partial_\theta v|_{r=a+g} \\
 &= (a+g)^2 d \partial_{r'} u|_{r'=a} - (\partial_{\theta'} g)(d-g) \partial_{\theta'} v|_{r'=a} \\
 &\quad + (\partial_{\theta'} g)^2 d \partial_{r'} v|_{r'=a},
 \end{aligned}$$

where we have used (2.10) to change coordinates. Solving for $\nu(\theta')$, we find

$$\begin{aligned}
 \nu &= a \partial_{r'} u + 2g \partial_{r'} u + \frac{1}{a} g^2 \partial_{r'} u - \frac{1}{a} (\partial_{\theta'} g) \partial_{\theta'} u + \frac{1}{ad} g (\partial_{\theta'} g) \partial_{\theta'} u \\
 (3.4) \quad &+ \frac{1}{a} (\partial_{\theta'} g)^2 \partial_{r'} u + \frac{a-d}{ad} g \nu + \frac{1}{ad} g^2 \nu,
 \end{aligned}$$

where all u quantities are evaluated at $r' = a$. Setting $g = \varepsilon f$, this normal current in the new coordinates can also be shown to be analytic in ε [20, 24, 25] so that

$$\nu(\theta', \varepsilon) = \sum_{n=0}^{\infty} \nu_n(\theta') \varepsilon^n,$$

and (3.4) can be used to show that

$$\begin{aligned}
 \nu_n &= a \partial_{r'} u_n + 2f \partial_{r'} u_{n-1} + \frac{1}{a} f^2 \partial_{r'} u_{n-2} - \frac{1}{a} (\partial_{\theta'} f) \partial_{\theta'} u_{n-1} \\
 (3.5) \quad &+ \frac{1}{ad} f (\partial_{\theta'} f) \partial_{\theta'} u_{n-2} + \frac{1}{a} (\partial_{\theta'} f)^2 \partial_{r'} u_{n-2} + \frac{a-d}{ad} f \nu_{n-1} + \frac{1}{ad} f^2 \nu_{n-2},
 \end{aligned}$$

where terms with negative index are set to zero.

3.4. Cancellations. It is a well-established phenomenon [21, 22, 23, 24, 25] that boundary perturbation algorithms such as the FE approach of section 2.2 are numerically ill-conditioned, due to subtle but significant cancellations present in the recursions whereby finite quantities are computed as differences of nearly equal, but arbitrarily large, numbers. For a brief demonstration of this property in the present context we consider the diagnostic calculation outlined in section 3.1 for a specified profile to high perturbation order.

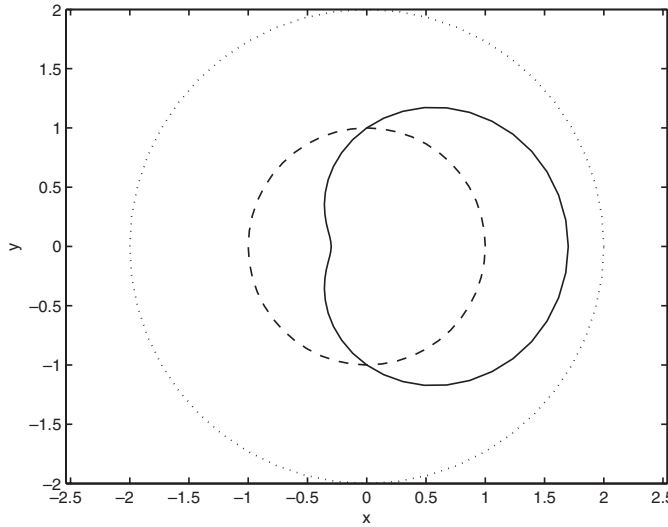


FIG. 3.1. Geometry of a scattering configuration with smooth perturbation, $f(\theta) = \cos(\theta)$, $\varepsilon = 0.7$. The scattering profile is given by the solid line, and the artificial boundary at $r = 2$ is depicted with the dotted line. The dashed line portrays the unperturbed scatterer at $r = 1$.

For an FE approximation we compute the $d_{n,p}$ of (2.8) using the recursion (2.9) for $-N_\theta/2 \leq p \leq N_\theta/2 - 1$ and $0 \leq n \leq N$. With these coefficients we approximate ν by

$$(3.6) \quad \nu^N(\theta, \varepsilon) = \sum_{n=0}^N \nu_n(\theta) \varepsilon^n,$$

where we use (3.3) to compute ν_n . For a TFE simulation we generate the $u_j^{(p)}$ (cf. (2.23)) from the algorithm outlined in section 2.4 for $-N_\theta/2 \leq p \leq N_\theta/2 - 1$, $0 \leq j \leq N_r - 2$, and $0 \leq n \leq N$. Again, with these coefficients we approximate ν by (3.6); however, we now use (3.5) to compute the ν_n .

In Figure 3.1 we display the geometry of a numerical experiment where we consider a large ($\varepsilon = 0.7$, $a = 1$) but smooth deformation, $f(\theta) = \cos(\theta)$, of a circle with artificial boundary at $r = b = 2$. The results of this experiment are summarized in Figure 3.2 with measurements of L^∞ error versus perturbation order N . The numerical parameters are $N_\theta = 48$, $N_r = 48$, and $N = 23$, and the frequency is $k = 1$, while the parameter p in (3.1) is set to one. We point out the abrupt and explosive divergence of the FE approximation from the exact solution beyond $N = 7$. In contrast, the TFE simulation gives progressively more accurate answers throughout all orders N . In particular, we note that the best answer that the FE method can ever deliver has L^∞ accuracy of 10^{-1} (when $N = 7$), while the TFE method gives answers reliable to 10^{-4} (at $N = 23$). As demonstrated in [22, 24], while the *qualitative* features of Figure 3.2 are quite generic as a function of profile size (ε) and shape (f), the *quantitative* details of the plot (e.g., divergence order of FE, slope of convergence for TFE, etc.) can be manipulated by an astute choice of ε and f .

Of course there are many questions one can ask regarding the cancellations present in the FE recursions. For instance, one can ask whether an “extended precision” implementation of the FE recursions could prevent the divergence witnessed in Figure 3.2, resulting in a reliable high-order method. In fact, this precise implementation was

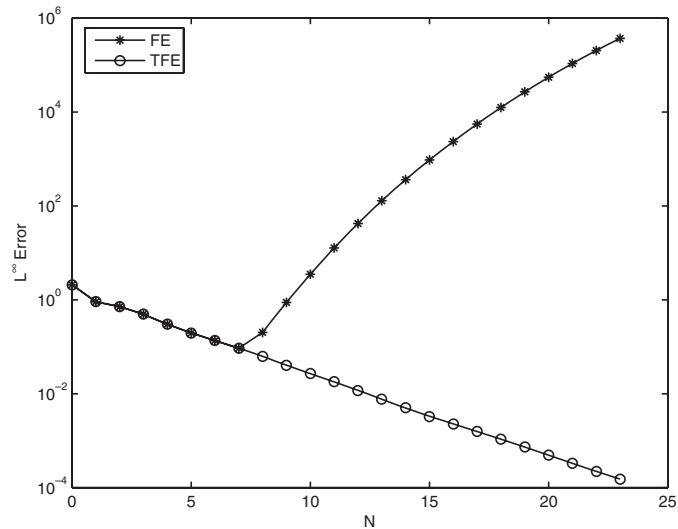


FIG. 3.2. L^∞ -norm of difference between exact current at the surface of a scatterer and the numerical approximation, versus perturbation order N . Both the FE (stars) and TFE (circles) approximations are plotted for the smooth perturbation $f(\theta) = \cos(\theta)$, $\varepsilon = 0.7$, with parameters $N_\theta = 48$, $N_r = 48$, $N = 23$, $a = 1$, $b = 2$, $k = 1$, $p = 1$. Notice the abrupt divergence of the FE approximation beyond $N = 7$ and the predictable, progressive convergence of the TFE approach throughout all orders.

made for the FE recursions in the related context of traveling water waves in [26]. For this problem *sextuple* precision calculations were necessary to display the strong cancellations present in this problem. From these experiments we learned that extended precision can *delay* the onset of divergent behavior but will never eliminate it. Furthermore, with the computational cost of current software implementations of extended precision it was *never* computationally advantageous to use the FE recursions. We direct the interested reader to [21, 22, 23, 24, 25, 26] (particularly [24]) for a complete discussion of these issues and their resolution.

4. Numerical results: Plane-wave scattering. In this section we present the results of numerical experiments conducted with the TFE method of section 2.3 in a variety of physical configurations. At this point we abandon the convenient “diagnostic test” calculations described in section 3.1 and return to our original problem of plane-wave scattering. Of course in this scenario there are no exact solutions for nontrivial geometries, so we appeal to a high-order integral equation (IE) method (Maue’s method; see [13, 9]) to provide an “exact solution.” We first investigate the performance of the TFE method as the frequency of radiation is increased from low to moderate values, and then study its behavior as the size and smoothness of the obstacle perturbation are changed from small to large and from smooth to rough.

4.1. Padé approximation. Before we describe our plane-wave numerical experiments we comment on one final enhancement to our algorithm: analytic continuation via Padé approximation. Recall that the TFE method computes a spectral approximation to the current, ν , of the form (cf. (3.6))

$$\nu_{N_\theta}^N(\theta, \varepsilon) = \sum_{n=0}^N \sum_{p=-N_\theta/2}^{N_\theta/2-1} a_{n,p} e^{ip\theta} \varepsilon^n = \sum_{p=-N_\theta/2}^{N_\theta/2-1} S_p^N(\varepsilon) e^{ip\theta}$$

TABLE 4.1
Summary of numerical experiments.

Experiment number	Profile type	k	ε	q	N_{IE}
1	Sinusoidal	1	0.1	4	128
2	Sinusoidal	10	0.1	4	256
3	Sinusoidal	50	0.1	4	1024
4	Sinusoidal	1	0.3	4	256
5	Sinusoidal	1	0.1	16	1024
6	Star-like	1	N.A.	N.A.	N.A.

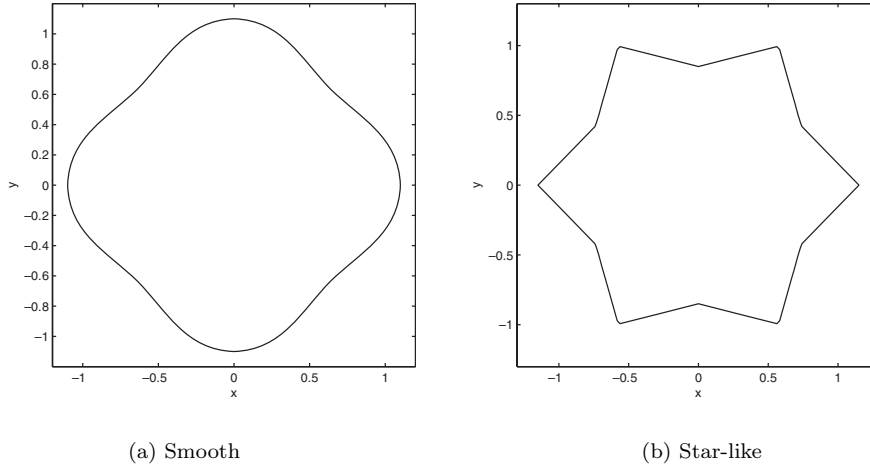


FIG. 4.1. Shape of smooth (cf. (4.2) with $\varepsilon = 0.1$ and $q = 4$) and star-like scatterers.

for ε small, where $S_p^N(\varepsilon)$ is the truncated Taylor series of the p th Fourier coefficient $S_p(\varepsilon)$. The analytic continuation results of [23, 20] indicate that the functions $S_p(\varepsilon)$ can be extended beyond the disk of convergence of their power series about $\varepsilon = 0$; a numerical technique for this analytic continuation is the Padé approximation method [1]. We recall that the $[P, Q]$ Padé approximant to a series

$$(4.1) \quad S(\varepsilon) = \sum_{n=0}^{\infty} a_n \varepsilon^n$$

is the unique rational function of order P over Q , which coincides with $S(\varepsilon)$ to order $P + Q + 1$. In the experiments below we use diagonal or paradiagonal Padé sequences. It is well known that Padé approximants have some remarkable properties of approximation of (a large subclass of) analytic functions from their Taylor series (4.1) for points far outside their radii of convergence; see, e.g., [1]. They can be calculated by first solving a set of linear equations for the denominator coefficients, and then using simple formulas to compute the numerator coefficients.

4.2. Numerical experiments. We now report upon six numerical experiments of plane-wave scattering, which are summarized in Table 4.1. In the first five the obstacle shape is quite smooth, in fact a sinusoidal perturbation of a circle, described by the equation

$$(4.2) \quad r = a + \varepsilon f_q(\theta), \quad f_q(\theta) = \cos(q\theta);$$

see Figure 4.1(a) ($q = 4$, $\varepsilon = 0.1$, and $a = 1$). The final experiment features a very rough, Lipschitz, scatterer of “star-like” shape; see Figure 4.1(b).

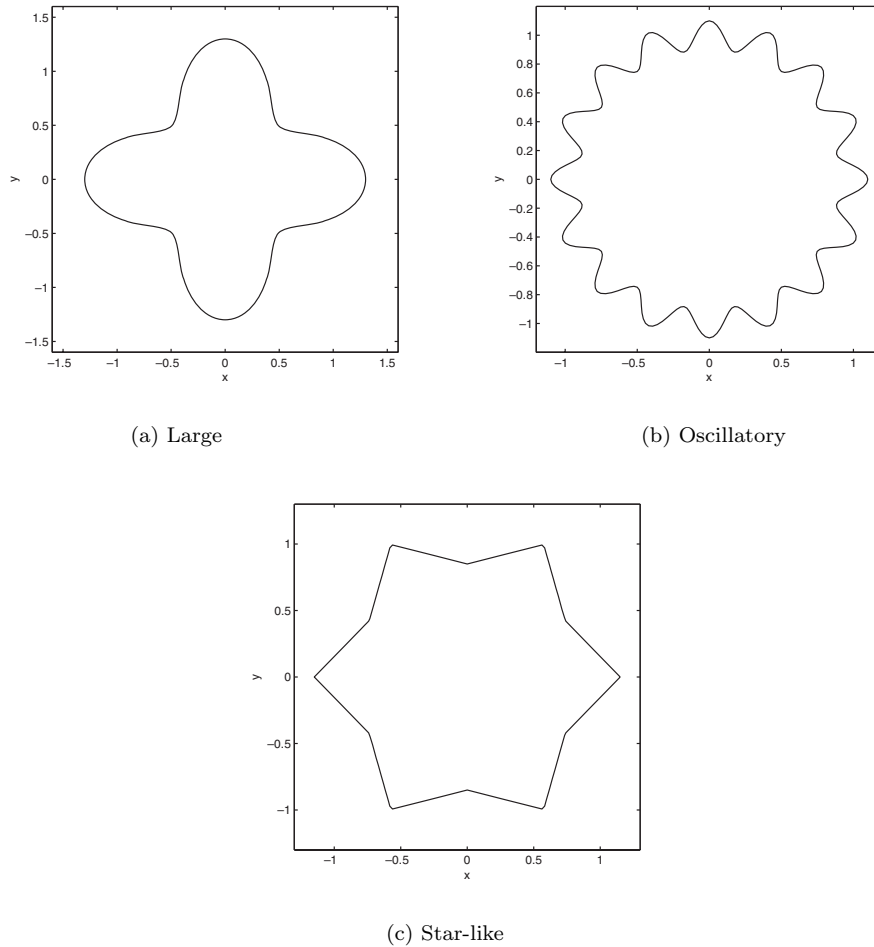


FIG. 4.2. Shape of large (cf. (4.2) with $\varepsilon = 0.3$ and $q = 4$), oscillatory ((4.2) with $\varepsilon = 0.1$ and $q = 16$), and star-like scatterers.

In the first three experiments we study the performance of the TFE method as the plane-wave frequency is increased from low to moderate. For this we use a small/smooth obstacle ($\varepsilon = 0.1$ and $q = 4$ in (4.2); see Figure 4.1(a) with $k = 1, 10$, and 50). In the final three experiments we gauge the capabilities of the TFE algorithm as the regularity of the obstacle is changed. We consider large/smooth ($\varepsilon = 0.3$ and $q = 4$), small/oscillatory ($\varepsilon = 0.1$ and $q = 16$), and Lipschitz (star-like) profiles for these experiments; see Figure 4.2.

In the final column of Table 4.1 we report the minimum number of discretization points necessary to guarantee a “well-resolved” IE approximation for each experiment. To measure the accuracy of the IE solution we compute the relative error in a “factor of two” refinement of an IE computation:

$$E_{\text{rel}}^N = \frac{|\nu_N^{IE} - \nu_{N/2}^{IE}|}{|\nu_N^{IE}|},$$

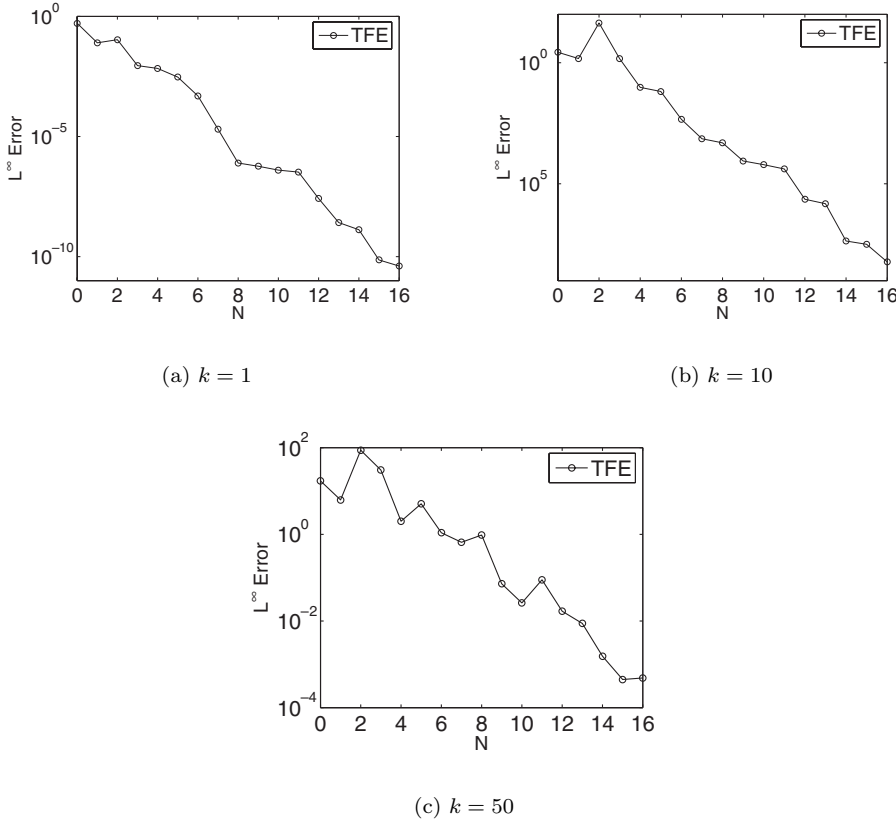


FIG. 4.3. L^∞ -norm of difference between highly resolved IE approximation of current at the surface of a scatterer and TFE approximation, versus perturbation order N . The shape of the scatterer is specified by (4.2) ($\epsilon = 0.1$ and $q = 4$), and the wavenumbers of the incident radiation are $(\alpha, \beta) = (1, 0)$, $(10, 0)$, and $(50, 0)$, in subfigures (a), (b), and (c), respectively.

where ν_N^{IE} represents an IE approximation to the surface current with N discretization points. The N_{IE} listed in the final column of Table 4.1 is the smallest N such that

$$E_{\text{rel}}^N < 10^{-10}.$$

4.2.1. Variation of frequency. The results of our first set of experiments (as the frequency is varied from low to moderate) are summarized in Figure 4.3. The physical and numerical parameters for each experiment are collected in Table 4.2; note that, for uniformity, in the first experiment we actually use more discretization points than necessary in the IE solver. In each of these experiments we note that the TFE algorithm makes steady improvement (as compared to the IE exact solution) as the perturbation order is refined. In the cases $k = 1, 10,$ and 50 , accuracies of $10^{-10}, 10^{-9},$ and 10^{-4} , respectively, are realized by $N = 16$; furthermore it is *necessary* to utilize these higher perturbation orders in order to realize this accuracy. In addition, a quite modest number of degrees of freedom are all that is required to properly resolve each configuration. Based upon the findings of [34] and the numerical results of section 2.4, we anticipate no problems simulating situations with k very large, as our new algorithm is numerically well-conditioned as *all* discretization parameters

TABLE 4.2

Summary of physical and numerical parameters: variation of frequency experiments ($q = 4$ and $\varepsilon = 0.1$).

Experiment number	k	a	b	N_θ	N_r	N	$N(IE)$
1	1	1	2	96	24	16	256
2	10	1	2	128	32	16	256
3	50	1	1.2	320	50	16	1024

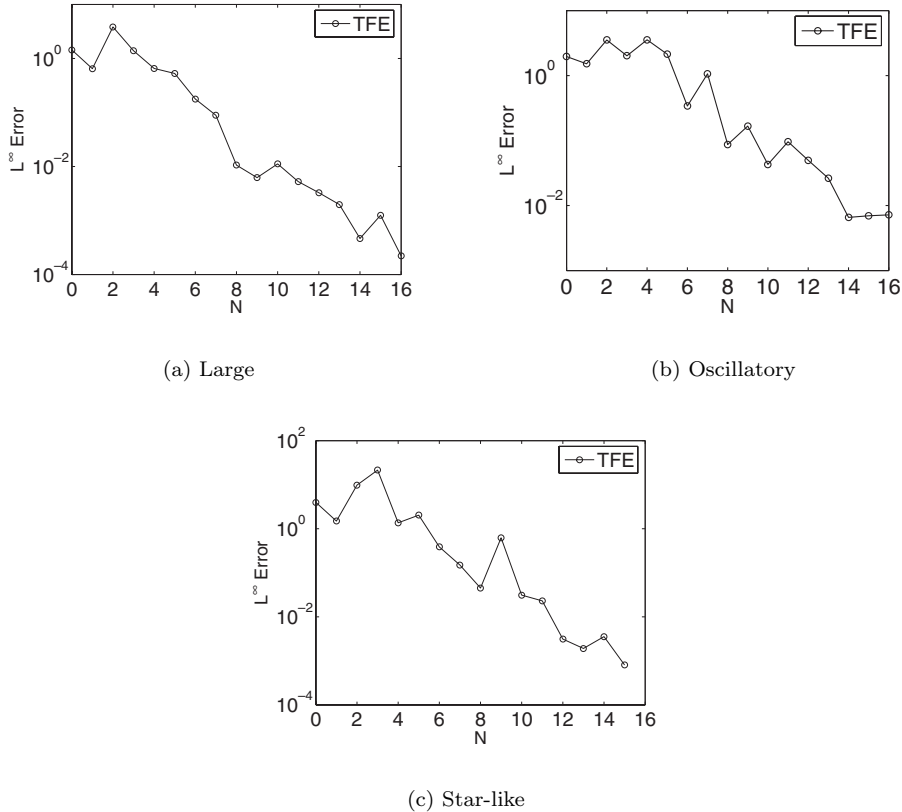


FIG. 4.4. (a) and (b) L^∞ -norm of difference between highly resolved IE approximation of current at the surface of a scatterer and TFE approximation, versus perturbation order N . The wavenumber of the incident radiation is $(\alpha, \beta) = (1, 0)$. The shapes of the scatterers are specified by (4.2) ((a): $\varepsilon = 0.3$ and $q = 4$; (b): $\varepsilon = 0.1$ and $q = 16$). (c) Cauchy convergence of TFE approximation measured in the L^∞ -norm as a function of perturbation order N . The wavenumber of the incident radiation is $(\alpha, \beta) = (1, 0)$. The shape of the scatterer is depicted in Figure 4.1(b).

(N_θ , N_r , and N) are refined. We note, however, that our method is not “specially designed” for the high-frequency regime in the manner of, e.g., [2].

4.2.2. Variation of shape. In the second set of experiments we recall that the frequency is fixed to be quite small ($k = 1$) while the profile shape is varied. For depictions of the scatterers for Experiments 4 (large/smooth profile), 5 (small/oscillatory profile), and 6 (Lipschitz profile) please see Figures 4.2(a), 4.2(b), and 4.2(c), respectively.

The results of these experiments are summarized in Figure 4.4. We note that for

TABLE 4.3

Summary of physical and numerical parameters: variation of shape experiments ($k = 1$).

Experiment number	ε	q	a	b	N_θ	N_r	N	$N(IE)$
4	0.3	4	1	2	256	48	16	256
5	0.1	16	1	2	256	48	16	1024
6	N.A.	N.A.	1	2	256	48	16	N.A.

the final simulation a different, “Cauchy,” measure of convergence was utilized due to the Lipschitz character of the star-like profile. In this case the IE solver cannot be used without nontrivial modification, so in order to avoid this issue (essentially that of quickly and accurately resolving quadratures involving singular kernels), we focus upon the TFE algorithm and measure, again in L^∞ , the difference between the TFE approximation at orders $0 \leq n < N$ and the “best resolution” TFE approximation at order N . The physical and numerical parameters for these experiments are collected in Table 4.3.

Once again we point out the consistent improvement which the TFE algorithm makes for all profiles at every perturbation order. For each profile we realize errors *at least* on the order of 10^{-2} by $N = 16$. This convergence is quite independent of the obstacle shape, although, of course, the *rate* of convergence does deteriorate with increasing roughness of the profile. Notice that this remains true even in the case of the Lipschitz profile, which we simply approximate by a truncated Fourier series. Again, each of these simulations could be further refined in a numerically stable fashion by increasing any of the algorithm parameters, N_θ , N_r , or N .

5. Conclusion and future directions. We have developed and implemented a stable, high-order method for numerical simulation of two-dimensional bounded-obstacle scattering. The method consists of five steps: (a) The problem (naturally posed on an unbounded domain) is reduced to one stated on a bounded domain via the Dirichlet–Neumann operator; (b) as suggested by previous theoretical work, this bounded domain is then mapped to an annulus; (c) a boundary perturbation expansion is then performed on the transformed equations, leading to a sequence of nonhomogeneous, constant-coefficient Helmholtz equations on the annulus; (d) an efficient and stable spectral-Galerkin method is developed for solving this sequence of Helmholtz problems; (e) Padé approximation is used to enhance and extend the summation of the power series representations we have formed. The resulting algorithm is shown to be very efficient and capable of handling small to moderate frequencies and scatterers with quite complex shapes.

The preliminary success of this TFE algorithm, of course, raises several natural questions which we consider as future directions for our research. It is clear that the basic ingredients of our numerical method can be extended to not only three-dimensional, bounded-obstacle configurations but also high-frequency problems in two and three dimensions. However, what is unclear is how this algorithm will compare with the popular finite element and integral equation methodologies already present in the literature. The highly accurate and efficient TFE algorithm together with its essentially *exact* treatment of far-field boundary conditions should make it a competitive choice compared with finite element approaches, particularly at moderate to high frequencies. On the other hand, its ability to seamlessly address problems with distributed sources will make this algorithm a compelling alternative to integral equation schemes. It is our intention to conduct an exhaustive study along these lines in future work.

Acknowledgments. The authors thank Fernando Reitich for providing a MATLAB script implementing the integral equations solver (Maue's method) for plane-wave scattering. They would also like to thank three anonymous referees for their thoughtful comments.

REFERENCES

- [1] G. A. BAKER, JR., AND P. GRAVES-MORRIS, *Padé approximants*, 2nd ed., Cambridge University Press, Cambridge, UK, 1996.
- [2] O. P. BRUNO, C. A. GEUZAINÉ, J. A. MONRO, JR., AND F. REITICH, *Prescribed error tolerances within fixed computational times for scattering problems of arbitrarily high frequency: The convex case*, Philos. Trans. R. Soc. Lond. Ser. A Math. Phys. Eng. Sci., 362 (2004), pp. 629–645.
- [3] O. P. BRUNO AND F. REITICH, *Solution of a boundary value problem for the Helmholtz equation via variation of the boundary into the complex domain*, Proc. Roy. Soc. Edinburgh Sect. A, 122 (1992), pp. 317–340.
- [4] O. P. BRUNO AND F. REITICH, *Numerical solution of diffraction problems: A method of variation of boundaries*, J. Opt. Soc. Amer. A, 10 (1993), pp. 1168–1175.
- [5] O. P. BRUNO AND F. REITICH, *Numerical solution of diffraction problems: A method of variation of boundaries. II. Finitely conducting gratings, Padé approximants, and singularities*, J. Opt. Soc. Amer. A, 10 (1993), pp. 2307–2316.
- [6] O. P. BRUNO AND F. REITICH, *Numerical solution of diffraction problems: A method of variation of boundaries. III. Doubly periodic gratings*, J. Opt. Soc. Amer. A, 10 (1993), pp. 2551–2562.
- [7] O. P. BRUNO AND F. REITICH, *Calculation of electromagnetic scattering via boundary variations and analytic continuation*, Appl. Comput. Electromagn. Soc. J., 11 (1996), pp. 17–31.
- [8] O. P. BRUNO AND F. REITICH, *Boundary-variation solutions for bounded-obstacle scattering problems in three dimensions*, J. Acoust. Soc. Amer., 104 (1998), pp. 2579–2583.
- [9] D. COLTON AND R. KRESS, *Inverse Acoustic and Electromagnetic Scattering Theory*, 2nd ed., Springer-Verlag, Berlin, 1998.
- [10] L. DEMKOWICZ AND F. IHLENBURG, *Analysis of a coupled finite-infinite element method for exterior Helmholtz problems*, Numer. Math., 88 (2001), pp. 43–73.
- [11] I. HARARI AND T. J. R. HUGHES, *Analysis of continuous formulations underlying the computation of time-harmonic acoustics in exterior domains*, Comput. Methods Appl. Mech. Engrg., 97 (1992), pp. 103–124.
- [12] P. J. KACZKOWSKI AND E. I. THORSOS, *Application of the operator expansion method to scattering from one-dimensional moderately rough Dirichlet random surfaces*, J. Acoust. Soc. Amer., 96 (1994), pp. 957–972.
- [13] A.-W. MAUE, *Zur Formulierung eines allgemeinen Beugungsproblems durch eine Integralgleichung*, Z. Phys., 126 (1949), pp. 601–618.
- [14] D. M. MILDER, *An improved formalism for rough-surface scattering of acoustic and electromagnetic waves*, in Proceedings of SPIE - The International Society for Optical Engineering (San Diego, 1991), vol. 1558, SPIE, Bellingham, WA, 1991, pp. 213–221.
- [15] D. M. MILDER, *An improved formalism for wave scattering from rough surfaces*, J. Acoust. Soc. Amer., 89 (1991), pp. 529–541.
- [16] D. M. MILDER, *An improved formalism for electromagnetic scattering from a perfectly conducting rough surface*, Radio Sci., 31 (1996), pp. 1369–1376.
- [17] D. M. MILDER, *Role of the admittance operator in rough-surface scattering*, J. Acoust. Soc. Amer., 100 (1996), pp. 759–768.
- [18] D. M. MILDER AND H. T. SHARP, *Efficient computation of rough surface scattering*, in Mathematical and Numerical Aspects of Wave Propagation Phenomena (Strasbourg, 1991), SIAM, Philadelphia, PA, 1991, pp. 314–322.
- [19] D. M. MILDER AND H. T. SHARP, *An improved formalism for rough surface scattering. II: Numerical trials in three dimensions*, J. Acoust. Soc. Amer., 91 (1992), pp. 2620–2626.
- [20] D. P. NICHOLLS AND N. NIGAM, *Exact non-reflecting boundary conditions on general domains*, J. Comput. Phys., 194 (2004), pp. 278–303.
- [21] D. P. NICHOLLS AND F. REITICH, *A new approach to analyticity of Dirichlet-Neumann operators*, Proc. Roy. Soc. Edinburgh Sect. A, 131 (2001), pp. 1411–1433.
- [22] D. P. NICHOLLS AND F. REITICH, *Stability of high-order perturbative methods for the computation of Dirichlet-Neumann operators*, J. Comput. Phys., 170 (2001), pp. 276–298.

- [23] D. P. NICHOLLS AND F. REITICH, *Analytic continuation of Dirichlet-Neumann operators*, Numer. Math., 94 (2003), pp. 107–146.
- [24] D. P. NICHOLLS AND F. REITICH, *Shape deformations in rough surface scattering: Cancellations, conditioning, and convergence*, J. Opt. Soc. Amer. A, 21 (2004), pp. 590–605.
- [25] D. P. NICHOLLS AND F. REITICH, *Shape deformations in rough surface scattering: Improved algorithms*, J. Opt. Soc. Amer. A, 21 (2004), pp. 606–621.
- [26] D. P. NICHOLLS AND F. REITICH, *On analyticity of traveling water waves*, Proc. Roy. Soc. London Ser. A, 461 (2005), pp. 1283–1309.
- [27] LORD RAYLEIGH, *On the dynamical theory of gratings*, Proc. Roy. Soc. London Ser. A, 79 (1907), pp. 399–416.
- [28] F. REITICH AND K. TAMMA, *State-of-the-art, trends, and directions in computational electromagnetics*, CMES Comput. Model. Eng. Sci., 5 (2004), pp. 287–294.
- [29] S. O. RICE, *Reflection of electromagnetic waves from slightly rough surfaces*, Comm. Pure Appl. Math., 4 (1951), pp. 351–378.
- [30] J. SHEN, *Efficient spectral-Galerkin method. I. Direct solvers of second- and fourth-order equations using Legendre polynomials*, SIAM J. Sci. Comput., 15 (1994), pp. 1489–1505.
- [31] J. SHEN, *Efficient spectral-Galerkin method. II. Direct solvers of second- and fourth-order equations using Chebyshev polynomials*, SIAM J. Sci. Comput., 16 (1995), pp. 74–87.
- [32] J. SHEN, *Efficient spectral-Galerkin methods. III. Polar and cylindrical geometries*, SIAM J. Sci. Comput., 18 (1997), pp. 1583–1604.
- [33] J. SHEN, *Efficient spectral-Galerkin methods. IV. Spherical geometries*, SIAM J. Sci. Comput., 20 (1999), pp. 1438–1455.
- [34] J. SHEN AND L.-L. WANG, *Spectral approximation of the Helmholtz equation with high wave numbers*, SIAM J. Numer. Anal., 43 (2005), pp. 623–644.
- [35] K. F. WARNICK AND W. C. CHEW, *Numerical simulation methods for rough surface scattering*, Waves Random Media, 11 (2001), pp. R1–R30.